ACS APPLIED NANO MATERIALS
Article
Cite This: ACS Appl. Nano Mater. 2019, 2, 3444−3452
www.acsanm.org

Excitation of Strong Localized Surface Plasmon Resonances in Highly Metallic Titanium Nitride Nano-Antennas for Stable Performance at Elevated Temperatures

Mena N. Gadalla,* Andrew S. Greenspon, Michele Tamagnone, Federico Capasso, and Evelyn L. Hu

John A. Paulson School of Engineering and Applied Sciences, Harvard University, Cambridge, Massachusetts 02138, United States

Web-Enhanced Feature *Supporting Information*

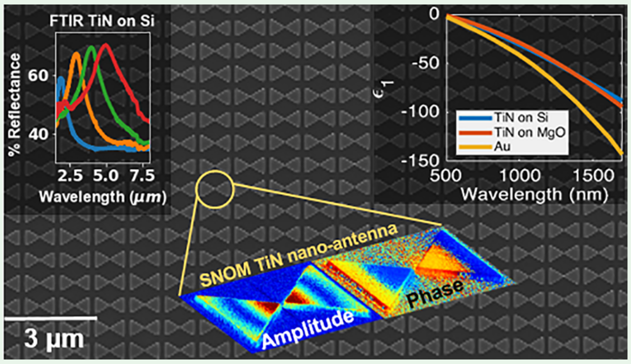

ABSTRACT: New opportunities for plasmonic applications at high temperatures have stimulated interest in refractory plasmonic materials that show greater stability at elevated temperatures than the more commonly used silver and gold (Au). Titanium nitride (TiN) has been identified as a promising refractory material, with deposition of TiN thin films through techniques ranging from plasma-enhanced atomic laser deposition to sputter deposition to pulsed laser deposition, on a variety of substrates, including MgO, polymer, SiO_2, and sapphire. A variety of plasmonic devices have been evaluated, including gratings, nanorods, and nanodisks. An implicit metric for TiN behavior has been the comparison of its plasmonic performance to that of Au, in particular at various elevated temperatures. This paper carries out a one-to-one comparison of bowtie nanoantennas formed of TiN and Au (on both Si and MgO substrates), examining the far-field characteristics, related to the measured near-field resonances. In both cases, the optical constants of the TiN films were used to simulate the expected plasmonic responses and enjoyed excellent agreement with the experimental measurements. Furthermore, we examined the consistency of the plasmonic response and the morphological changes in the TiN and Au nanoantennas at different temperatures up to 800 °C in the atmosphere. This comparison of the measured plasmonic response from nanoscale resonances to the far-field response allows for anomalies or imperfections that may be introduced by the nanofabrication processes and provides a more accurate comparison of TiN plasmonic behavior relative to the Au standard.

KEYWORDS: *refractory materials, titanium nitride, plasmonic nanoantennas, near-field enhancement, localized surface plasmons, Fourier transform infrared spectroscopy, scattering type scanning near-field optical microscopy, high temperature thermo-plasmonic*

INTRODUCTION

The field of plasmonics has enjoyed rapid growth in the past 20 years, with a broad set of applications including surface enhanced Raman spectroscopy,[1−3] “super-resolution” imaging of objects below the diffraction limit of light,[4] holography,[5] biosensing and catalysis,[6,7] and nano-optics.[8,9] As applications for plasmonic devices have grown, so has the requirement for stable and robust plasmonic materials that exhibit consistent plasmonic behavior at higher temperatures than the more conventionally used materials such as gold and silver. Higher-temperature plasmonic applications include heat-assisted magnetic recording,[10] broadband metamaterial absorbers,[11] computer chips,[12,13] photothermal imaging,[14,15] energy harvesting,[16] and drug delivery and cancer treatment.[17,18] Titanium nitride (TiN) has been identified as a promising plasmonic material, with the ability to withstand higher temperatures, and is also biocompatible.[19] As a highly promising candidate for plasmonic applications, TiN has been deposited on a range of substrate materials including sapphire, MgO, SiO_2, and a polymer[20] through deposition techniques that range from sputter deposition[21−24] to plasma-enhanced atomic laser deposition[25] to pulsed laser deposition.[20] A variety of plasmonic devices have been evaluated, including gratings,[21] nanorods,[26] and nanodisks.[25] Previous reports have examined the stability and expected optical performance of TiN at high temperatures.[22,26,27]

An implicit metric for TiN behavior has been the comparison of its plasmonic performance to Au, in particular at elevated temperatures. This paper carries out an integrated and one-to-one comparison of bowtie nanoantennas formed of TiN and Au on both Si and MgO substrates, examining both far-field characteristics and their relationship to the measured near-field resonances. To ensure the most robust outcomes of the measurements, the nanoantennas were designed with

Received: February 27, 2019
Accepted: May 7, 2019
Published: May 22, 2019

DOI: 10.1021/acsanm.9b00370
ACS Appl. Nano Mater. 2019, 2, 3444−3452

optimized geometries to maximize expected far-field reflections at the intended resonance wavelength. For both near- and far-field simulations, the optical constants of the TiN films were used to simulate the expected plasmonic responses and enjoyed excellent agreement with the experimental measurements. Furthermore, we examined the consistency of the plasmonic response and the morphological changes in the TiN and Au nanoantennas at different temperatures up to 800 °C in the atmosphere. Therefore, we carried out detailed and calibrated measurements of the plasmonic performance of both TiN and Au nanostructures after being annealed at several high temperatures in the air. We related these to the morphological changes in the material at each temperature using X-ray photoelectron spectroscopy (XPS) analysis. This comparison of measured plasmonic response from nanoscale resonances to far-field response allows for anomalies or imperfections that may be introduced by the nanofabrication processes and provides a more accurate plasmonic behavior relative to the performance of Au.

A metric related to the plasmonic or metallic behavior of TiN is the magnitude of the negative, real part of the material permittivity ($\mathrm{Re}(\varepsilon)$). Values of $\mathrm{Re}(\varepsilon)$ at 1700 nm wavelength have been reported as ranging from -20 to -90, for TiN films deposited on different substrates and under different deposition conditions.[21,24,20,27,28] MgO and sapphire substrates have been frequently employed substrates for the deposition of plasmonic TiN. Our own earlier work,[29] utilizing sputter deposition at room temperature, produced highly metallic TiN thin films with values of $\mathrm{Re}(\varepsilon)$ reaching -85 and -75 at 1700 nm for MgO and sapphire substrates, respectively, and only moderately metallic TiN on Si with values of $\mathrm{Re}(\varepsilon)$ reaching -40 at 1700 nm. We believed that the advantage of MgO substrates, compared to Si or sapphire, was a better lattice match of MgO to TiN. However, crystalline order alone was not the sole predictor of plasmonic behavior since films deposited on MgO at room temperature showed better plasmonic properties than those deposited at 600 °C,[29,30] where the STEM images of the latter films exhibited better lattice matching. Therefore, while the substrate and its possible templating role can influence the resulting properties of the overlying plasmonic thin film, the concomitant details of the deposition temperature and the substrate bias also determine the performance of the thin film. Thus, changing the deposition conditions for different substrates influences the film composition, stoichiometry, and density,[31] and thus the electronic and optical properties of the TiN film. These results suggest the possibility of further optimization of the deposition conditions to produce more highly metallic TiN on MgO or sapphire and on new alternative substrates such as Si. The present work augments these previous reports to demonstrate the production of very highly metallic TiN films with the highest reported plasmonic figure of merit ($\mathrm{FOM} = -\varepsilon_1/\varepsilon_2$) formed on Si and MgO substrates. We were able to optimize the sputter-deposition process to maximize the metallicity of the thin films for different substrates. This produces values of $\mathrm{Re}(\varepsilon)$ very close to those of Au regardless of the substrate underneath, suggesting the possibility of adjusting deposition conditions to form high plasmonic-quality TiN on a large variety of substrates.

Figure 1 shows the deposition process of our TiN thin films. We used a variety of sputter-deposition conditions, including higher temperature deposition at different values of applied DC bias and different ratios of argon to nitrogen. In particular, 80 nm of TiN was sputtered onto <100> P-silicon (boron doped, 5×10^{19} cm^{-3}), at a substrate temperature of 700 °C, a 200 V applied substrate bias, and a ratio of argon to nitrogen equal to 12:8 sccm. In addition, 80 nm of TiN was sputtered onto <100> MgO, at a substrate temperature of 650 °C, a 120 V applied substrate bias, and a ratio of argon to nitrogen equal to 12:4 sccm. The deposition pressure was held at 4 mTorr for both samples with a base pressure of around 5×10^{-8} Torr. Ellipsometric measurements were made using a Woollam WVASE32 vertical angle spectroscopic rotating-analyzer ellipsometer to determine the frequency-dependent complex dielectric function of the sputtered TiN thin films. The measurements were taken at three different incidence angles of 55°, 65°, and 75°. At each angle, the wavelength was varied from 300 to 1700 nm in steps of 5 nm. Fits to the data were made using a Drude-Lorentz[32,33] model comprising a Drude oscillator representing the free d-band conduction electrons[31] and two Lorentz oscillators representing the inter- and intraband losses. Figure 2a and b show the resulting plots of the real and imaginary part of the permittivity (ε) for TiN on MgO and TiN on Si. Also shown are the corresponding plots for Au thin films deposited on Si and MgO using electron beam evaporation, using values for ε of Au from ref 34. Optical properties and FOMs of different Au thin films from different references can be found in Figure S1 in the Supporting Information. Figure 2 indicates that Au has the maximum negative $\mathrm{Re}(\varepsilon)$ and the minimum positive value of $\mathrm{Im}(\varepsilon)$, resulting in the excellent plasmonic performance of Au thin film nanostructures. However, also apparent are the nearly equal negative values of $\mathrm{Re}(\varepsilon)$ for TiN on MgO and TiN on Si and the slightly higher values of $\mathrm{Im}(\varepsilon)$, compared to Au. Thus,

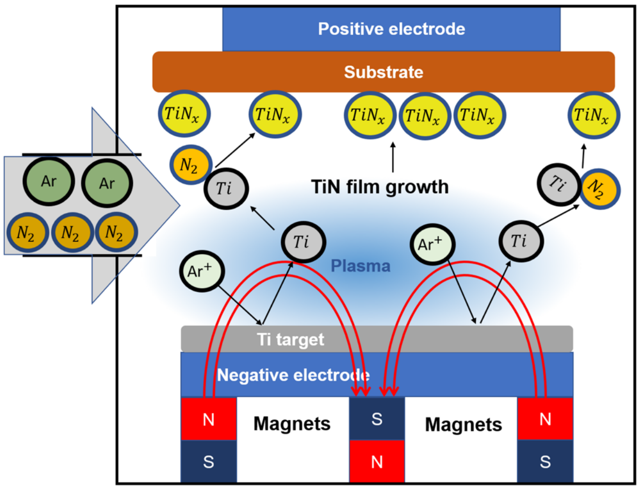

Figure 1. TiN thin film sputter deposition process showing the flow of a mixture of argon and nitrogen gases into the sputtering chamber under a high vacuum. The magnetic field (red lines) produced by the magnets installed below the negative electrode ionizes the argon atoms into positive ions creating a plasma cloud of argon ions around the target. The ions then get accelerated and attracted toward the negatively charged electrode, resulting in multiple collision events with the titanium target, ejecting titanium atoms into the chamber. These sputtered titanium atoms combine with the flowing nitrogen atoms to form TiN_x that gets deposited onto the substrate. The stoichiometry and the optical properties of the resulting film depend on the ratio of argon to nitrogen, applied substrate bias through the positive electrode, and applied substrate temperature through an internal heater below the substrate that is installed on the substrate holder inside the sputtering chamber.

DOI: 10.1021/acsanm.9b00370
ACS Appl. Nano Mater. 2019, 2, 3444−3452

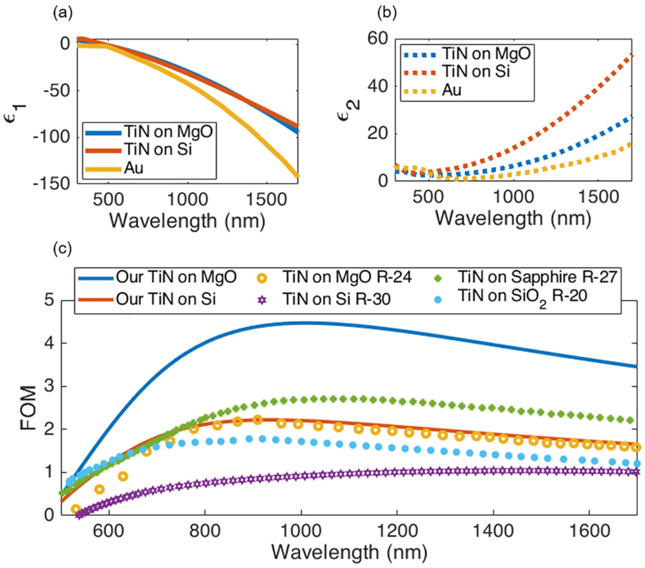

Figure 2. (a) Real and (b) imaginary part of the dielectric function of Au and of our sputtered TiN thin films on Si and MgO substrates. The data are obtained by spectroscopic ellipsometry and show strong metallic character of TiN thin films with Re(ε) values of TiN on Si being very close to those of TiN on MgO and Au. (c) Figure of merit (FOM = $-\varepsilon_1/\varepsilon_2$) for different TiN films from this work (brown and blue curves) and recent TiN films reported in refs 20, 24, 27, and 30.

we have separately optimized the deposition conditions for TiN on MgO and on Si substrates to obtain large negative values of Re(ε) in both cases, equal to each other and slightly smaller (in absolute value) than the case for Au. While Re(ε) is comparable for TiN on MgO and TiN on Si, the imaginary part of the dielectric function of TiN on Si is higher than that of TiN on MgO. Re(ε) relates to the free electron density in the material, and we optimized the deposition conditions in both cases to achieve the maximum negative value of Re(ε), implying a relatively high electron density in the TiN thin films regardless of the type of the substrate. However, Im(ε) relates to the mechanisms of loss in the material, such as might result from structural defects or impurities. The subtleties of loss mechanisms require far greater and more sensitive analysis of the thin films and characteristic defects or impurities that may be incorporated as a result of the type of the substrate used and the deposition conditions. These optical data both suggest the possibility of tuning TiN deposition conditions to obtain high negative Re(ε) on a variety of substrates and also suggest a plasmonic performance that is comparable to that of Au thin films. As a comparison, in Figure 3c, we plot the FOMs for our TiN films, in comparison to the recently reported values for TiN on different substrates.

In order to make calibrated comparisons of the TiN plasmonic response to corresponding structures in Au, we analyzed the performance of nanobowtie antenna arrays fabricated from Au on Si and TiN on Si (data for nanoantenna arrays of TiN on MgO and Au on MgO are presented in the Supporting Information). Au nanoantenna arrays were formed on Si and MgO by evaporation of 80-nm-thick Au thin films through an electron-beam-patterned poly(methyl methacrylate) (PMMA495-C6) mask. Fabrication of TiN nanoantennas on Si and MgO substrates utilized e-beam-patterned negative resist comprising hydrogen silsesquioxane (HSQ) and ma-N 2400 MicroChem, Inc. Following e-beam lithography, a dry etching process was used to transfer the pattern from the resist to the TiN thin film. A flowchart of the different fabrication processes is given in the Supporting Information (Figure S2). There may be concerns that the different processing techniques used to fabricate the TiN and Au nanoantennas might lead to different surface morphologies and/or surface residues. In order to avoid uncertainties in the direct comparison of the optical responses of TiN and Au nanoantennas, we conducted a set of FTIR measurements to show that exposing the Au nanoantennas' surfaces to the same resist as the TiN nanoantennas (HSQ negative tone resist) would not affect the optical results. HSQ resist was applied to our Au nano-antennas on silicon, and the entire array was exposed to the same electron beam dose as used for the TiN antennas. Resist development and removal was carried out in the same way as done for the TiN nanoantennas. The FTIR spectrum for the Au nanoantenna array before and after the HSQ process did not display a difference in optical response. Thus, we believe the comparisons of TiN and Au nanoantenna responses to be reasonable, although the fabrication processes differed. Nanoantenna arrays of different spacings and different sizes were formed, with the bowtie side lengths ranging from 200 nm to 2 μm (Figure 3a). The TiN and Au nanobowtie antennas comprised two equilateral triangles, where the minimum side length of the triangle is 200 nm with a minimal gap of 20 nm (Figure 3b).

Figure 3b illustrates the design parameters, P_x, P_y (distances between array elements in x and y, respectively) and h (the arm height of the nanoantenna) that were used for the arrays. The gaps between bowtie tips are 50 nm in all cases. The intention was to choose optimized values of design parameters

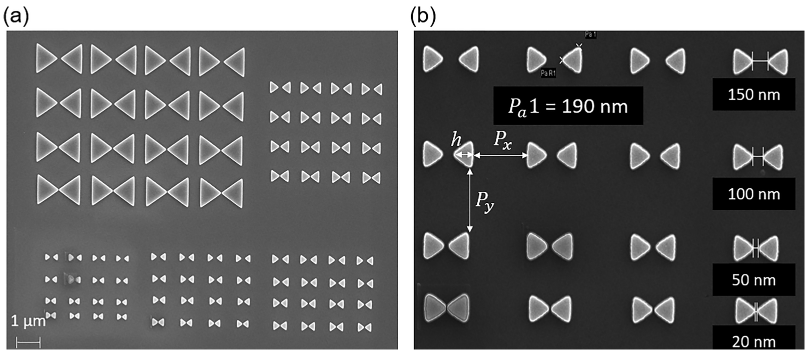

Figure 3. (a) SEM image of TiN bowtie nanoantenna arrays on Si with well-defined gaps and different side lengths (200 nm, 300 nm, 400 nm, 500 nm, and 1 μm). (b) 200 nm side length TiN antenna array on Si with gaps ranging from 150 to 20 nm.

so that we could systematically and clearly measure plasmonic resonance responses for wavelengths ranging from 1.5 to 6 μm. We therefore carried out FDTD simulations of the far-field reflection spectra from an array of nanoantennas and the expected near-field enhancement for isolated antennas (Figure S6 in the Supporting Information) in the wavelength range between 1.5 and 6 μm. In order to model TiN plasmonic performance, data such as those shown in Figure 2 were extrapolated to the mid-IR range and imported to the commercial package Lumerical FDTD Solutions. For each simulation scenario, we used a Particle Swarm Optimization (PSO) algorithm[35] to find starting values for P_x, P_y, and h that maximize the reflection at the intended resonance wavelength. We also studied the sensitivity of the reflection curve to small variations in each parameter to finalize the geometries to be fabricated, concluding with seven optimized designs (termed Array 1−Array 7) for P_x, P_y, and h that can maximize and tune the plasmonic coupling resonances in the far-field between 1.5 and 6 μm. More details about the FDTD simulation models are presented in the Supporting Information.

FTIR measurements (Figure 4) produced far-field reflection spectra from nanoantenna arrays made of TiN on Si and Au on Si. For each set of nanoantenna parameters (h, P_x, P_y), a 35 μm × 50 μm array of nanoantennas was fabricated, an array size larger than the spot size of the FTIR. The samples were introduced to the beam path from a broadband light source made of silicon carbide (SiC), and the far-field FTIR spectrum was collected in the wavenumber range from 6500 to 1250 cm^{-1} with 4 cm^{-1} resolution. Each nanoarray measurement comprised 150 scans with the aperture size set to 25 μm × 40 μm. Baseline corrections were carried out to compensate for wavelength-independent background light scattering. Further details about the FTIR experiments and baseline corrections can be found in the Supporting Information. Figure 4c confirms the excellent surface plasmon response of the Au on Si nanoantennas with ~80% resonantly enhanced reflectivity. Figure 4a, by comparison, illustrates the distinctive and robust TiN nanoantenna resonances with only slightly reduced (compared to Au) reflectivities, evidence of the excellent plasmonic performance of TiN nanoantennas. Furthermore, comparisons between Figure 4 and b and between Figure 4c and d illustrate an excellent agreement between experimental results and FDTD simulations. The agreement between the simulations and measurements provides validation for the optical properties modeling of our plasmonic TiN thin films and highlights the tunability of resonant response with nanoantenna geometry. Qualitatively similar results (Figure S3 in the Supporting Information) were shown in a comparison of TiN nanoantennas on MgO substrates, compared to Au on MgO, also showing excellent agreement between simulations and experimental results.

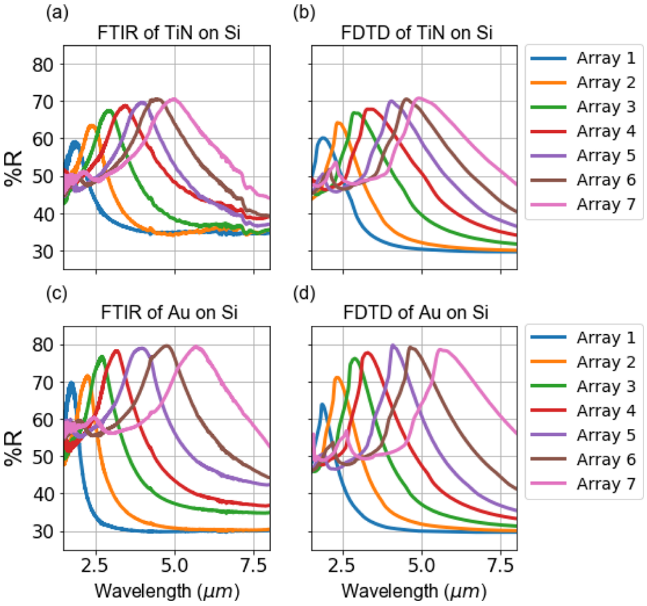

Figure 4. Matching experimental and simulated FTIR spectra from seven geometrically different nanoantenna arrays made of (a,b) TiN and (c,d) Au on Si substrate. Each array exhibits a distinct plasmonic resonance highlighting the similarities between nanostructures made of Au and TiN in supporting highly tunable resonant enhanced scattering plasmonic peaks. h ranges from 300 nm in array 1 to 1000 nm in array 7 with a step of 100 nm. P_x and P_y range from 80 nm in array 1 to 240 nm in array 7.

While the far-field resonant response of the TiN nanoantennas is slightly reduced from that of Au, we anticipate that the high-temperature performance of TiN would be superior. To validate this hypothesis, we performed another set of FTIR measurements after annealing arrays of both Au and TiN nanoantennas in the air at temperatures of 400 °C, 600 °C, and 800 °C. One array was comprised of Au on Si (h = 740 nm, P_x = 300 nm, P_y = 320 nm), and another was comprised of TiN on Si (h = 750 nm, P_x = 240 nm, P_y = 270 nm). For each annealing step, we used a cylindrical furnace that was ramped up to the desired temperature and left to equilibrate before introducing the TiN and the Au samples simultaneously. After 10 min of annealing at the desired temperature, the samples were removed and left to cool down to room temperature. This heating protocol was implemented to detect the direct effect of annealing on the plasmonic response of the nanostructures and to identify the annealing conditions at which the TiN plasmonic response is more stable than that of Au. Since degradation in the Au nanoantennas was apparent after only 10 min of annealing, that time set the limit of our annealing period. We are aware that longer annealing times can result in degradation of the TiN plasmonic thin films at temperatures lower than 600 °C. A fuller treatment of thermal stability of TiN and other plasmonic thin films at longer annealing times is provided by Wells et al. and others.[36−38] Figure 5a tracks the plasmonic performance of the TiN nanoantenna array as a function of temperature. The plasmonic resonance of the TiN nanoantennas and the shape of the curve remains similar at room temperature, 400 °C, and 600 °C.

At 600 °C, there is a slight shift in the peak position and percentage reflection for the TiN nanoantennas, due to the formation of a thin titanium oxide layer, which appears as dark orange coloration in the inset of Figure 5c-iii. This was confirmed by the SEM images presented in the insets of Figures 5c-i,ii,iii showing almost no noticeable change in the microscopic appearance of TiN nanoantennas granules for temperatures less than or equal to 600 °C.

At 800 °C, we observed a distinct change in the microscopic appearance of the granules of the TiN nanoantennas (Figure 5c-iv), reflecting the changes in the composition of the TiN due to annealing, suggesting a transformation from metallic titanium nitride to a dielectric material, resulting from the oxidation of the TiN. This can also be seen in the change of

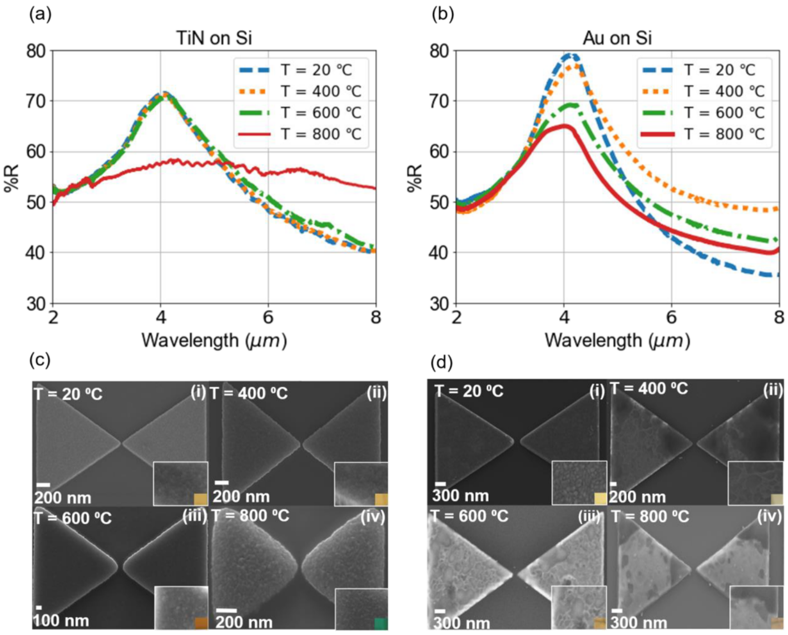

Figure 5. FTIR experiments of (a) annealed TiN nanoantenna array in the atmosphere at different temperatures. The FTIR spectra from the TiN nanoantenna array at room temperature and after annealing at 400 °C are almost the same, indicating that there is no oxidation or structural changes in the TiN nanoantennas until 400 °C. We attribute the slight change in the shape of the reflection spectrum after annealing at 600 °C to the formation of a thin titanium oxide layer on the surface of the antennas. (b) Annealed Au nanoantenna array in the atmosphere at different temperatures showing significant variability of the plasmonic resonance frequency and the plasmonic coupling intensity at different temperatures. (c) SEM images of the TiN nanoantennas at (i) room temperature, (ii) 400 °C, (iii) 600 °C, and (iv) 800 °C. (d) SEM images showing severe microscopic degradation in Au nanoantennas at high temperatures (ii, iii, iv) causing shifts in the resonance frequency. The insets show high magnification SEM images of the granules in addition to corresponding color of the (c) TiN and (d) Au thin films after each annealing step.

color of the TiN thin film from gold-like at room temperature to green at 800 °C (inset of Figure 5c-iv). This material transformation manifests itself in the complete loss of the plasmonic resonance in the FTIR spectrum (red curve in Figure 5a) of the TiN nanoantennas after annealing at 800 °C. The observations regarding the formation of a larger component of titanium oxide at successively higher annealing temperatures (800 °C) and a thin oxide layer at 600 °C were confirmed by employing X-ray photoelectron spectroscopy (XPS) analysis (see Supporting Information Figure S4) on four different TiN thin film samples shown in the insets of Figure 5c; one sample was unannealed, and the rest were annealed at 400 °C, 600 °C, and 800 °C in the air. The XPS analysis revealed the formation of a 10 nm oxide layer at 600 °C. By incorporating a 10 nm titanium oxide layer in our simulations (Figure S5 in the Supporting Information), we were able to replicate the spectral shift observed in the green curve in Figure 5a. On the other hand, the TiN film annealed at 800 °C completely transformed to rutile titanium dioxide with no traces of nitrogen in the thin film. Very similar microscopic changes and oxidation behavior of TiN thin films at high temperatures have been reported before.[39]

For annealing temperatures less than 600 °C, the consistency of the TiN film composition and invariance of the plasmonic resonance frequency and intensity detected by FTIR confirm the excellent robustness of the TiN nanoantennas. In comparison, the plasmonic resonance frequency of Au antennas fluctuates significantly at high temperatures as shown in Figure 5b. Additionally, we observed significant microscopic material degradation in the Au nanoantennas after annealing at 400 °C. Figure 5d shows SEM images of Au nanoantennas at 20 °C, 400 °C, 600 °C, and 800 °C. The images show that this degradation increased as we increased the annealing temperature until the antennas started melting at 1000 °C. Because the Au degradation is initiated at relatively low temperatures, the corresponding plasmonic performance is modified. This is evident in the variation of the plasmonic resonance frequency, in addition to the attenuation of the peak intensity, as shown in Figure 5b, among the antennas annealed at different temperatures. The insets of Figure 5c and d compare the colors of the TiN thin film on Si and Au thin film on Si annealed at different temperatures. The changes in color of the TiN film to dark orange at 600 °C and light green at 800 °C is due to the oxidation process that starts at 600 °C and consumes the TiN completely at 800 °C. This study seeks to make a direct comparison of the performance of highly metallic TiN nanoantennas formed on the electronically predominant Si substrates, compared to the corresponding Au nanoantennas. While the plasmonic performance of Au serves as standard for evaluation of the TiN nanoantenna performance, the relatively high diffusivity and solubility of Au in Si has been previously well-recognized.[40] We expect that the high temperature performance of Au nanoantennas on other substrates such as MgO or glass may not encounter the same challenges of interdiffusivity or solubility, but nevertheless, the lower melting temperature for Au (~1000 °C) compared to TiN (~3000 °C) will still provide an advantage for TiN nanoantennas operating under conditions of higher temperature or higher incident power. Furthermore, similar observations regarding high temperature degradation of Au thin films and their metallicity (optical properties) on different substrates, other than Si, have been reported before.[41,42]

The far-field data shown in Figure 4 provide convincing evidence that both TiN and Au nanoantennas on silicon

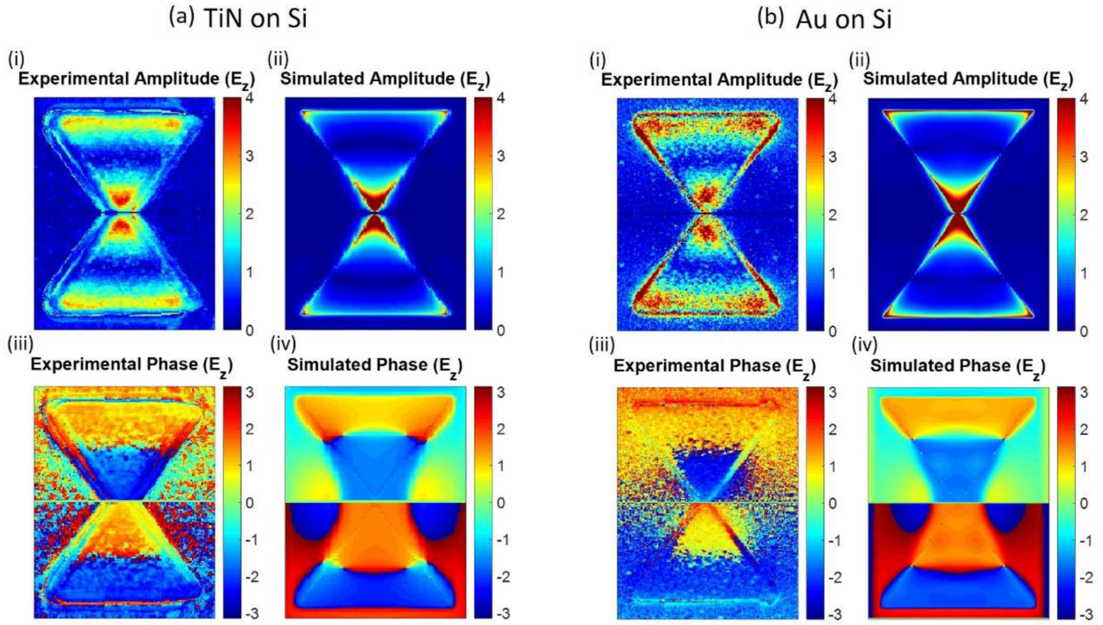

Figure 6. Resonant near-field localized surface plasmon modes in (a) TiN and (b) Au nanoantennas on Si showing the strong interaction between the exciting electromagnetic waves and the nanostructures. (i) S-SNOM measured amplitude of the out of plane E-field component on the surface of (a-i) TiN on Si and (b-i) Au on Si nanoantenna showing very similar near-field enhancement capabilities. (ii) Simulated near-field amplitude on the surface of (a-ii) TiN and (b-ii) Au single nanoantenna in FDTD with E-field polarization parallel to the antenna axis with optical properties adapted from Figure 2. (iii) Phase heat maps of the out of plane E-field component on the surface of (a-iii) TiN on Si and (b-iii) Au on Si nanoantenna ranging from $-\pi$ to π showing a strong dipolar bright mode evident in the 180° phase shift across the gap. (iv) FDTD simulations of the S-SNOM measurements for the phase of (a-iv) TiN on Si and (b-iv) Au on Si nanoantenna showing excellent agreement with the measurements.

exhibit distinctive and highly tunable plasmonic resonances in the near to mid-IR region. Further validation is found in spatially resolved near-field images of strongly coupled localized surface plasmon modes in TiN and Au nanoantenna structures. We obtained such images by carrying out apertureless Scattering-type Scanning Near-field Optical Microscopy (S-SNOM) measurements on optimized TiN and Au nanoantenna structures. These measurements also confirm the plasmonic and field enhancement equivalence between Au on Si and our TiN on Si. Our S-SNOM analysis utilized a silicon tip coupled to an atomic force microscopy (AFM) system, allowing for high spatial resolution 3D movement of the tip around the nanoantennas.

For these experiments, four individual antennas (TiN on Si, Au on Si, TiN on MgO, and Au on MgO) were designed and fabricated to exhibit a strong dipolar localized surface plasmon resonance and maximize the near-field intensity enhancement in the nanogap for mid-infrared illumination at about 6 μm wavelength, the wavelength used in the S-SNOM measurements. On the basis of FDTD simulations for the near-field intensity enhancement in the middle of the gap between the bowtie arms, the maximum localized surface plasmon resonance for TiN and Au on Si occurs for a bowtie arm h of 0.7 μm. Similar simulations for the MgO case are presented in Figure S6 in the Supporting Information. The nanoantenna is illuminated by a 6 μm wavelength light source (a narrow-band quantum cascade laser, QCL) through a Michelson interferometer at an incidence angle of 60°. The silicon tip, in tapping mode on the sample, gets polarized by the laser source and itself acts as a local antenna that scatters the near-field from the surface of the nanostructures, modulating the light with the tapping frequency. A moving mirror, oscillating at the same frequency as the tip, is used to implement pseudo-heterodyne demodulation of the phase and amplitude of the scattered field. Images of phase and amplitude, such as those shown in Figure 6a-i and a-iii, are formed by raster scans of the tip over the antenna's surface in the (x,y) plane. This setup, similar to that described in ref 43, allows for the detection of the magnitude and phase of the out-of-plane electric field component (E_z) only. A complication for this measurement lies in the polarization of the tip itself by the laser source. As a result, the scattered fields are modulated by the tip oscillations, and the resulting near-field heat maps are a superposition of the actual LSP mode to be imaged and other contributions coming from the tip itself locally exciting the structure, coupling light into it as the tip raster scans the surface of the nanostructures. Because the FDTD simulations do not take the moving tip effect into consideration, the raw images need to be processed to remove the unwanted tip-launched components. As done in ref 43, we can extract the mode field (which has odd symmetry) by subtracting the complex field image from its flipped replica, thus removing the tip-launched components that have even symmetry. Figure 6 shows the processed S-SNOM images for amplitude and phase of E_z on the surface of the TiN on Si (left column) and Au on Si (right column) bowtie nanoantennas. In each case, the correspondence between experimental measurements and FDTD simulations is excellent. The data for TiN on MgO and Au on MgO bowtie nanoantennas are shown in the Supporting Information.

The heat maps of Figure 6 reveal that TiN on Si and Au on Si exhibit LSPs with the same spatial distribution of both amplitude and phase and with very similar intensities. For both TiN and Au, we observe very similar values for the enhanced localized field amplitude toward the tips of the bowtie, especially concentrated at the gaps. The resolved electric field phase shows a strong dipolar LSP mode with a 180° phase jump from one bowtie arm to the other right across the gap. That strong oscillating electric dipole on the surface of the antenna produces the resonantly enhanced scattering that we observe in the far-field FTIR experiments. The radiation from this oscillating dipole leads to resonantly enhanced scattering of the incoming plane wave by the nanoantennas, which can be represented as an array of point dipoles. Results for similar S-SNOM experiments for TiN and Au nanoantennas on a MgO substrate (Figure S7 in the Supporting Information) confirm the significant similarity between the LSP near-field distribution and intensity of TiN and Au nanoantennas. The good agreement between the experimental S-SNOM amplitudes and phases with the simulated results validate the values we use in modeling the optical properties of the TiN, as well as the algorithm employed to extract the field phase and field amplitude from the S-SNOM measurements. Figure 6 represents a 2D time average of the plasmon resonance (amplitude and phase) obtained by S-SNOM near-field measurements. Web Enhanced Objects (WEOs) showing the 3D temporal evolution of the real part of the resonant plasmon mode obtained by S-SNOM measurements for both TiN and Au nanoantennas on silicon can be viewed by clicking on the appropriate caption text for Figure 6a and b, respectively. Similar videos showing the temporal oscillations of the dipole for TiN and Au nanoantennas on MgO can be found in the Supporting Information.

To further confirm that the S-SNOM measurements demonstrate a resonant plasmon phenomenon, we fabricated two off-resonance structures with TiN and Au antennas with a bowtie height h of 1.1 μm for the MgO substrate and 1.5 μm for the Si substrate. The S-SNOM measurements and the FDTD simulations for these structures both exhibited a significant drop in the surface field amplitude as expected (results in the Supporting Information).

CONCLUSION

In conclusion, we produced a highly metallic TiN thin film on both Si and MgO substrates through separate optimization of the deposition conditions for each substrate. Such observations suggest the possibility of producing highly metallic TiN on a large variety of substrates, extending the range of TiN plasmonic applications. We have achieved high plasmonic quality TiN on Si with metallic behavior that is very similar to that of Au on Si. FTIR reflection spectra were used to analyze and compare the far-field performance of nanoantenna arrays made of TiN and Au. The TiN nanoantenna arrays showed highly tunable plasmonic peaks in the near to mid-IR range, specifically from 1.5 to 6 μm, resulting from changes in the dimensions and the periodic placement of the TiN nanoantenna array elements. Additionally, S-SNOM experiments were conducted to analyze the near-field distribution of the localized surface plasmon dipolar resonances in isolated TiN and Au nanobowtie antennas. These measurements showed that TiN nanostructures on Si and MgO exhibit the desired LSP modes, field enhancement, and localization capabilities that are very similar to those of Au on Si and MgO, respectively. Excellent agreement between FDTD simulations and our FTIR and S-SNOM measurements confirms the validity of the optical models used for our TiN plasmonic films. XPS depth-profiling revealed the effect of high temperature annealing in the air and confirmed the chemical stability of TiN nanoantennas up to 600 °C. These simulations and measurements conducted on TiN and Au nanoantennas in aggregate reveal the excellent, robust performance of TiN compared to Au. Such detailed, calibrated, and one-to-one comparisons of TiN and Au plasmonic responses are critical in a realistic evaluation of TiN or any new plasmonic material.

ASSOCIATED CONTENT

Supporting Information

The Supporting Information is available free of charge on the ACS Publications website at DOI: 10.1021/acsanm.9b00370.

> Figure S1: Comparison between the optical properties and FOM of our TiN thin films and different Au thin films. Figure S2: Fabrication process details and results for TiN and Au nanoantennas on Si and MgO. Figure S3: Comparison of the FTIR spectra for seven different arrays made of TiN and Au on MgO. Figure S4: XPS analysis of the TiN thin films annealed at different temperatures with the insets showing SEM cross section images of the annealed films. Figure S5: Effect of creation of 10 nm titanium dioxide on the plasmonic resonance. Figure S6: Comparison of optical near-field intensity enhancement due to LSP resonance in TiN and Au nanoantennas with different arm heights with a 50 nm gap. Figure S7: Complete S-SNOM and FDTD results for resonant TiN and Au nanoantennas on MgO. Figure S8: Complete S-SNOM and FDTD results for resonant TiN and Au nanoantennas on Si. Figure S9: Complete S-SNOM and FDTD results for off-resonant TiN and Au nanoantennas on MgO. Figure S10: Complete S-SNOM and FDTD results for off-resonant TiN and Au nanoantennas on Si (PDF)
>
> Video 1: Temporal evolution of the measured dipole induced near-field (real part of the instantaneous field) on the surface of TiN nanoantenna on MgO. Video 2: Temporal evolution of the measured dipole induced near-field (real part of the instantaneous field) on the surface of Au nanoantenna on MgO (ZIP)

Web-Enhanced Feature

The 3D temporal evolution of the real part of the resonant plasmon mode obtained by S-SNOM measurements for both TiN and Au nanoantennas on silicon seen in Figure 6a and b are available as video files.

AUTHOR INFORMATION

Corresponding Author

*E-mail: mgadalla@g.harvard.edu.

ORCID

Mena N. Gadalla: 0000-0002-5006-4403
Andrew S. Greenspon: 0000-0002-9631-7568
Michele Tamagnone: 0000-0002-9812-2449

Notes

The authors declare no competing financial interest.

ACKNOWLEDGMENTS

This work was performed in part at the Harvard University Center for Nanoscale Systems (CNS), a member of the National Nanotechnology Coordinated Infrastructure Network (NNCI), which is supported by the National Science Foundation under NSF ECCS award no. 1541959. M.T. acknowledges the support of the Swiss National Science

Foundation (SNSF) grant nos. 168545 and 177836. The authors gratefully acknowledge Amirhassan Shams-Ansari from the Loncar group at Harvard University for all his help and discussions on fabrication and Antonio Ambrosio at Harvard University Center for Nanoscale Systems (CNS) for his insightful contributions to the S-SNOM experiments.

REFERENCES

(1) Fleischmann, M.; Hendra, P. J.; McQuillan, A. J. Raman Spectra of Pyridine Adsorbed at a Silver Electrode. *Chem. Phys. Lett.* **1974**, *26* (2), 163−166.

(2) Moskovits, M. Surface Roughness and the Enhanced Intensity of Raman Scattering by Molecules Adsorbed on Metals. *J. Chem. Phys.* **1978**, *69* (9), 4159−4161.

(3) Jeanmaire, D. L.; Van Duyne, R. P. Surface Raman Spectroelectrochemistry: Part I. Heterocyclic, Aromatic, and Aliphatic Amines Adsorbed on the Anodized Silver Electrode. *J. Electroanal. Chem. Interfacial Electrochem.* **1977**, *84* (1), 1−20.

(4) Gramotnev, D. K.; Bozhevolnyi, S. I. Plasmonics Beyond the Diffraction Limit. *Nat. Photonics* **2010**, *4* (2), 83.

(5) Nelson, J. W.; Knefelkamp, G. R.; Brolo, A. G.; Lindquist, N. C. Digital Plasmonic Holography. *Light: Sci. Appl.* **2018**, *7* (1), 52.

(6) Anker, J. N.; Hall, W. P.; Lyandres, O.; Shah, N. C.; Zhao, J.; Van Duyne, R. P. Biosensing with Plasmonic Nanosensors. *Nat. Mater.* **2008**, *7* (6), 442−453.

(7) Nusz, G. J.; Curry, A. C.; Marinakos, S. M.; Wax, A.; Chilkoti, A. Rational Selection of Gold Nanorod Geometry for Label-Free Plasmonic Biosensors. *ACS Nano* **2009**, *3* (4), 795−806.

(8) Zayats, A. V.; Smolyaninov, I. I.; Maradudin, A. A. Nano-Optics of Surface Plasmon Polaritons. *Phys. Rep.* **2005**, *408* (3−4), 131−314.

(9) Pendry, J. B. Negative Refraction Makes a Perfect Lens. *Phys. Rev. Lett.* **2000**, *85* (18), 3966.

(10) Challener, W.; Peng, C.; Itagi, A.; Karns, D.; Peng, W.; Peng, Y.; Yang, X.; Zhu, X.; Gokemeijer, N.; Hsia, Y.-T.; Ju, G.; Rottmayer, R. E.; Seigler, M. A.; Gage, E. C. Heat-Assisted Magnetic Recording by a near-Field Transducer with Efficient Optical Energy Transfer. *Nat. Photonics* **2009**, *3* (4), 220.

(11) Yan, M. Metal−Insulator−Metal Light Absorber: A Continuous Structure. *J. Opt.* **2013**, *15* (2), 025006.

(12) Tang, L.; Kocabas, S. E.; Latif, S.; Okyay, A. K.; Ly-Gagnon, D.-S.; Saraswat, K. C.; Miller, D. A. Nanometre-Scale Germanium Photodetector Enhanced by a near-Infrared Dipole Antenna. *Nat. Photonics* **2008**, *2* (4), 226.

(13) Cai, W.; White, J. S.; Brongersma, M. L. Compact, High-Speed and Power-Efficient Electrooptic Plasmonic Modulators. *Nano Lett.* **2009**, *9* (12), 4403−4411.

(14) Boyer, D.; Tamarat, P.; Maali, A.; Lounis, B.; Orrit, M. Photothermal Imaging of Nanometer-Sized Metal Particles among Scatterers. *Science* **2002**, *297* (5584), 1160−1163.

(15) Zijlstra, P.; Paulo, P. M.; Orrit, M. Optical Detection of Single Non-Absorbing Molecules Using the Surface Plasmon Resonance of a Gold Nanorod. *Nat. Nanotechnol.* **2012**, *7* (6), 379−382.

(16) Gadalla, M.; Abdel-Rahman, M.; Shamim, A. Design, Optimization and Fabrication of a 28.3 Thz Nano-Rectenna for Infrared Detection and Rectification. *Sci. Rep.* **2015**, *4*, 4270.

(17) Saklayen, N.; Huber, M.; Madrid, M.; Nuzzo, V.; Vulis, D. I.; Shen, W.; Nelson, J.; McClelland, A. A.; Heisterkamp, A.; Mazur, E. Intracellular Delivery Using Nanosecond-Laser Excitation of Large-Area Plasmonic Substrates. *ACS Nano* **2017**, *11* (4), 3671−3680.

(18) Hirsch, L. R.; Stafford, R. J.; Bankson, J.; Sershen, S. R.; Rivera, B.; Price, R.; Hazle, J. D.; Halas, N. J.; West, J. L. Nanoshell-Mediated near-Infrared Thermal Therapy of Tumors under Magnetic Resonance Guidance. *Proc. Natl. Acad. Sci. U. S. A.* **2003**, *100* (23), 13549−13554.

(19) Guler, U.; Boltasseva, A.; Shalaev, V. M. Refractory Plasmonics. *Science* **2014**, *344* (6181), 263−264.

(20) Sugavaneshwar, R. P.; Ishii, S.; Dao, T. D.; Ohi, A.; Nabatame, T.; Nagao, T. Fabrication of Highly Metallic Tin Films by Pulsed Laser Deposition Method for Plasmonic Applications. *ACS Photonics* **2018**, *5* (3), 814−819.

(21) Naik, G. V.; Schroeder, J. L.; Ni, X.; Kildishev, A. V.; Sands, T. D.; Boltasseva, A. Titanium Nitride as a Plasmonic Material for Visible and near-Infrared Wavelengths. *Opt. Mater. Express* **2012**, *2* (4), 478−489.

(22) Li, W.; Guler, U.; Kinsey, N.; Naik, G. V.; Boltasseva, A.; Guan, J.; Shalaev, V. M.; Kildishev, A. V. Refractory Plasmonics with Titanium Nitride: Broadband Metamaterial Absorber. *Adv. Mater.* **2014**, *26* (47), 7959−7965.

(23) Naik, G. V.; Kim, J.; Boltasseva, A. Oxides and Nitrides as Alternative Plasmonic Materials in the Optical Range. *Opt. Mater. Express* **2011**, *1* (6), 1090−1099.

(24) Naik, G. V.; Saha, B.; Liu, J.; Saber, S. M.; Stach, E. A.; Irudayaraj, J. M.; Sands, T. D.; Shalaev, V. M.; Boltasseva, A. Epitaxial Superlattices with Titanium Nitride as a Plasmonic Component for Optical Hyperbolic Metamaterials. *Proc. Natl. Acad. Sci. U. S. A.* **2014**, *111* (21), 7546−7551.

(25) Briggs, J. A.; Naik, G. V.; Petach, T. A.; Baum, B. K.; Goldhaber-Gordon, D.; Dionne, J. A. Fully Cmos-Compatible Titanium Nitride Nanoantennas. *Appl. Phys. Lett.* **2016**, *108* (5), 051110.

(26) Gui, L.; Bagheri, S.; Strohfeldt, N.; Hentschel, M.; Zgrabik, C. M.; Metzger, B.; Linnenbank, H.; Hu, E. L.; Giessen, H. Nonlinear Refractory Plasmonics with Titanium Nitride Nanoantennas. *Nano Lett.* **2016**, *16* (9), 5708−5713.

(27) Reddy, H.; Guler, U.; Kudyshev, Z.; Kildishev, A. V.; Shalaev, V. M.; Boltasseva, A. Temperature-Dependent Optical Properties of Plasmonic Titanium Nitride Thin Films. *ACS Photonics* **2017**, *4* (6), 1413−1420.

(28) Guler, U.; Zemlyanov, D.; Kim, J.; Wang, Z.; Chandrasekar, R.; Meng, X.; Stach, E.; Kildishev, A. V.; Shalaev, V. M.; Boltasseva, A. Plasmonic Titanium Nitride Nanostructures Via Nitridation of Nanopatterned Titanium Dioxide. *Adv. Opt. Mater.* **2017**, *5* (7), 1600717.

(29) Zgrabik, C. M.; Hu, E. L. Optimization of Sputtered Titanium Nitride as a Tunable Metal for Plasmonic Applications. *Opt. Mater. Express* **2015**, *5* (12), 2786−2797.

(30) Zgrabik, C. M. Wide Tunability of Magnetron Sputtered Titanium Nitride and Titanium Oxynitride for Plasmonic Applications. Doctoral dissertation, Harvard University, 2016.

(31) Patsalas, P.; Logothetidis, S. Optical, Electronic, and Transport Properties of Nanocrystalline Titanium Nitride Thin Films. *J. Appl. Phys.* **2001**, *90* (9), 4725−4734.

(32) White, N.; Campbell, A.; Grant, J.; Pachter, R.; Eyink, K.; Jakubiak, R.; Martinez, G.; Ramana, C. Surface/Interface Analysis and Optical Properties of Rf Sputter-Deposited Nanocrystalline Titanium Nitride Thin Films. *Appl. Surf. Sci.* **2014**, *292*, 74−85.

(33) Rivory, J.; Behaghel, J.; Berthier, S.; Lafait, J. Optical Properties of Substoichiometric Tinx. *Thin Solid Films* **1981**, *78* (2), 161−165.

(34) Johnson, P. B.; Christy, R.-W. Optical Constants of the Noble Metals. *Phys. Rev. B* **1972**, *6* (12), 4370.

(35) Robinson, J.; Rahmat-Samii, Y. Particle Swarm Optimization in Electromagnetics. *IEEE Trans. Antennas Propag.* **2004**, *52* (2), 397−407.

(36) Wells, M. P.; Bower, R.; Kilmurray, R.; Zou, B.; Mihai, A. P.; Gobalakrichenane, G.; Alford, N. M.; Oulton, R. F.; Cohen, L. F.; Maier, S. A.; Zayats, A. V.; Petrov, P. K. Temperature Stability of Thin Film Refractory Plasmonic Materials. *Opt. Express* **2018**, *26* (12), 15726−15744.

(37) Briggs, J. A.; Naik, G. V.; Zhao, Y.; Petach, T. A.; Sahasrabuddhe, K.; Goldhaber-Gordon, D.; Melosh, N. A.; Dionne, J. A. Temperature-Dependent Optical Properties of Titanium Nitride. *Appl. Phys. Lett.* **2017**, *110* (10), 101901.

(38) Yin, Y.; Hang, L.; Zhang, S.; Bui, X. Thermal Oxidation Properties of Titanium Nitride and Titanium−Aluminum Nitride Materials—a Perspective for High Temperature Air-Stable Solar Selective Absorber Applications. *Thin Solid Films* **2007**, *515* (5), 2829−2832.

(39) Chen, H.-Y.; Lu, F.-H. Oxidation Behavior of Titanium Nitride Films. *J. Vac. Sci. Technol., A* **2005**, *23* (4), 1006−1009.

(40) Green, A.; Bauer, E. Formation, Structure, and Orientation of Gold Silicide on Gold Surfaces. *J. Appl. Phys.* **1976**, *47* (4), 1284−1291.

(41) Reddy, H.; Guler, U.; Kildishev, A. V.; Boltasseva, A.; Shalaev, V. M. Temperature-Dependent Optical Properties of Gold Thin Films. *Opt. Mater. Express* **2016**, *6* (9), 2776−2802.

(42) Kalachyova, Y.; Lyutakov, O.; Solovyev, A.; Slepička, P.; Švorčík, V. Surface Morphology and Optical Properties of Porphyrin/Au and Au/Porphyrin/Au Systems. *Nanoscale Res. Lett.* **2013**, *8* (1), 547.

(43) Tamagnone, M.; Ambrosio, A.; Chaudhary, K.; Jauregui, L. A.; Kim, P.; Wilson, W. L.; Capasso, F. Ultra-Confined Mid-Infrared Resonant Phonon Polaritons in Van Der Waals Nanostructures. *Science Advances* **2018**, *4* (6), eaat7189.